Real-time 3D position reconstruction of guidewire for monoplane X-ray

T. Petković [a,*], R. Homan [b], S. Lončarić [a]

[a] University of Zagreb, Faculty of Electrical Engineering and Computing, Unska 3, HR-10000 Zagreb, Croatia
[b] Philips Healthcare, 5680 DA Best, The Netherlands

A B S T R A C T

We present a novel real-time method for the 3D reconstruction of the guidewire using a monoplane X-ray. The method consists of two steps: (1) the backprojection step to reconstruct a 3D surface that contains the guidewire and (2) the optimization step to select a curve on the surface that is the best match under the pre-specified constraints. The proposed method utilizes a priori knowledge in the form of a volume that indicates positions of the blood vessels and thus restricts the reconstruction. The reconstruction precision is limited by the local thickness of the vessels. The method is quantitatively evaluated on five phantom datasets and qualitatively on two patient datasets. For the phantom datasets the average reconstruction error is resolution limited to 1–2 voxels and is biased in the depth direction. The worst-case reconstruction error for any point, including the guidewire tip, is not larger than the local vessel thickness. A visual inspection of results for the patient datasets shows the guidewire is always placed in the proper vessel and is aligned with the 2D image, which is sufficient for the guidewire navigation. The developed implementation achieves the processing speed of 12 fps using Core™ i7 CPU 920 at 2.67 GHz.

© 2013 Elsevier Ltd. All rights reserved.

1. Introduction

Computer aided intervention (CAI) plays an important role in modern medicine. CAI advantages include procedure simplification and duration reduction resulting in better patient outcomes. To achieve these advantages complex methods and apparatus are needed.

An important research problem are automated image analysis methods to assist the medical personnel conducting neuro-endovascular interventions that require insertion of a guidewire into a blood vessel. Accurate navigation of the guidewire is a prerequisite for a successful CAI. X-ray imaging modality is often used as a navigational aid to obtain the projected position of the guidewire (Fig. 1). Image-based guidewire tracking and 3D position reconstruction are required to provide a better insight into the true 3D position of the guidewire.

An automated guidewire tracking and 3D position reconstruction method for navigation must have the following properties: (1) *accurate* 3D guidewire tip tracking, (2) *robustness* to noise and imaging artifacts, and (3) *real-time* operation.

The paper is organized as follows: Section 2 gives an overview of the state of the art. In Section 3 the proposed guidewire reconstruction method is presented. The experimental validation is presented in Section 4. The reconstruction results and discussion are given in Section 5. The conclusion is given in Section 6. A brief description of some real-time issues is given in Appendix.

2. Background

Early work on guidewire tracking includes research by Zarge and Corby [37] who describe a scheme for 2D guidewire detection using heuristic operations on the Hessian matrix elements to identify the guidewire pixels followed by a graph-theoretical approach to join the pixels into a single line. Palti-Wasserman et al. [23] describe a semiautomatic system that utilizes the Hough transform for fitting a second order polynomial to the guidewire projection. A significant additional research is by Baert et al. [3] who describe an incremental spline fitting procedure utilizing both spatial and temporal information to track the guidewire in 2D. The method presented in [3] is extended to biplane tracking and 3D reconstruction by Baert et al. [2] using a straightforward reconstruction algorithm. Takemura et al. [32] describe a background subtraction method to detect the guidewire tip. Spiegel et al. [30] also use a Hessian matrix-based line detection approach for the 2D detection and augment the segmentation by linking the found line segments using the Dijkstra's algorithm. Bismuth et al. [6] compare three approaches to 2D line

* Corresponding author. Tel.: +385 1 6129563; fax: +385 1 6129652.
E-mail addresses: tomislav.petkovic.jr@fer.hr (T. Petković),
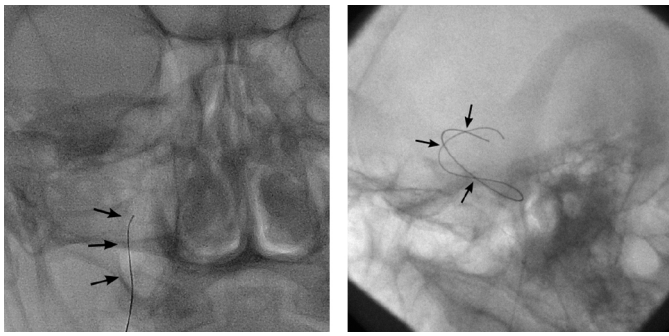robert.homan@philips.com (R. Homan), sven.loncaric@fer.hr (S. Lončarić).

Fig. 1. Fluoroscopic images typical for neuro-interventions. Guidewires are visible as thin dark lines.

detection for guidewire segmentation and conclude that the Hessian matrix-based methods are suitable for strongly curved lines, while the family of anisotropic rotated filters is suitable for low carrier-to-noise applications. Barbu et al. [4] present a learning-based method to segment the 2D guidewire, while Wang et al. [34] extend it to use a temporal coherence for continuous tracking. Mazouer et al. [20] also extend [4] to offline semiautomatic guidewire segmentation. Lessard et al. [18] present a 2D guidewire tracking method that separates the observed motion into forward and lateral components and thus captures the natural guidewire movement.

Of particular interest are solutions to the 3D position reconstruction problem for monoplane devices that are most common in practice. Most of the aforementioned research efforts, with the exception of [2], do not discuss the 3D reconstruction. To solve the inherent ambiguity of the 3D reconstruction for monoplane devices some additional knowledge must be used. Alternatively, a single C-arm imaging device could be used to obtain several projections of the stationary guide wire to reconstruct the 3D position as described in [2] or [26]. However, such an approach has a few undesirable properties: (a) the C-arm must be repositioned for each projection so the reconstruction is slower, (b) the C-arm movement might hinder the physicians, and (c) the guidewire must be stationary. Reconstruction methods using a single projection and some additional knowledge do not have these drawbacks at the price of reduced accuracy.

Of the monoplane 3D reconstruction methods described in the literature van Walsum et al. [33] present a method that uses a min-cost algorithm to select an appropriate solution and thus resolve the ambiguity. However, ambiguity and uncertainty of the reconstruction are not thoroughly addressed. This is especially true for applications where guidewire projections form complex self-intersecting shapes, e.g. neuro-interventions. Another interesting approach to the 3D position and orientation recovery applicable only for pre-shaped tip guidewires is described by Esthappan et al. [11], where a 2D/3D registration is used to find a rigid body transform to align the model of the tip to the 2D image.

In this paper, we present a method to reconstruct the 3D position of the guidewire within the blood vessels specifically developed for a monoplane X-ray device. The blood vessels are segmented from a pre-operative scan that is obtained with the same C-arm device and are represented by a 3D voxel dataset we call the restrictive volume (same dataset is used for roadmapping [29]). The guidewire is segmented in a 2D image sequence using both spatial and temporal analysis. Then for each input image the 3D position of the guidewire is reconstructed using the 2D guidewire segmentation and the restrictive volume. Additional information that is available if the input is a sequence of images with a time-varying viewpoint is not utilized for the 3D reconstruction; such sequence is treated as a set of independent images. Treating every image

independently removes the need to address the problem of rapid and discontinuous guidewire movement, which is most often caused by the non-uniform time intervals between image frames that are typical in practice to minimize the radiation dose. Due to non uniqueness of the 3D reconstruction the proposed method finds almost all suitable solutions of interest together with the 3D position uncertainties that are presented using an interactive display. The presented reconstruction method is specifically developed for a monoplane C-arm device with the main goal of it serving as a navigational tool during neuro CAI procedures.

A significant difference with respect to the previously proposed methods, such as the 3D reconstruction method described by van Walsum et al. [33], is in the representation of the 2D result as an unstructured set of pixels making any assumptions about the 2D projection unnecessary. Usually, the intermediate 2D result is represented as a parametrized curve, e.g. a spline, that is fitted to the pixel data. However, a 2D projection of the guidewire may have a complex shape showing both self-intersections and cusps. Both self-intersections and cusps interfere with the fitting process. Such shapes make currently proposed methods lacking as possible effects on 2D segmentation and tracking results are not addressed. The proposed method avoids this intermediate reconstruction step. Instead, we directly use the unstructured 2D segmentation result that can contain incorrectly segmented or disjoint pixels, and we delegate the problem of curve parametrization to the 3D processing stage allowing a more natural approach.

3. Methodology

The problem of guidewire reconstruction from a single view can be decomposed into two subproblems: (1) segmentation and tracking of the 2D guidewire in a single frame or in a sequence and (2) 3D reconstruction of the guidewire from a single 2D projection.

The first subproblem is well understood with many available solutions (listed in Sections 2 and 3.3). The second problem is ill-posed as the solution is not unique. To solve the 3D reconstruction ambiguity some additional knowledge about the problem is required, either in a form of a restrictive volume that limits possible curve positions in 3D or in a form of a 2D image sequence with a time-varying viewpoint.

3.1. Overview

The proposed method to reconstruct the guidewire from a single projection can be decomposed as shown in Fig. 2. It is composed of several stacked 2D detection methods whose results are joined together (Section 3.3) followed by a backprojection resulting in a sampled surface that contains the guidewire (Section 3.4). The guidewire is then reconstructed by an optimization procedure (Section 3.5).

3.2. Problem statement

Let $f : \mathbb{R} \rightarrow \mathbb{R}^3$ be a continuous smooth 3D curve (the guidewire) and let $g : \mathbb{R} \rightarrow \mathbb{R}^2$ be a 2D projection of f under known perspective transform. Let restrictive volume (the blood vessels) with an associated skeleton (a vessel tree) be a representation of the problem-specific knowledge. We consider the reconstruction problem: knowing the samples of g, the viewing geometry, and the restrictive volume with the associated skeleton find a 3D curve $\hat{f}$ placed inside the restrictive volume whose 2D projection matches the samples of g.

When discussing this problem the following questions should be addressed: (a) What can be inferred about existence and uniqueness of the reconstruction? (b) How does additional information, e.g. a restriction of allowed positions, aid the reconstruction? (c)
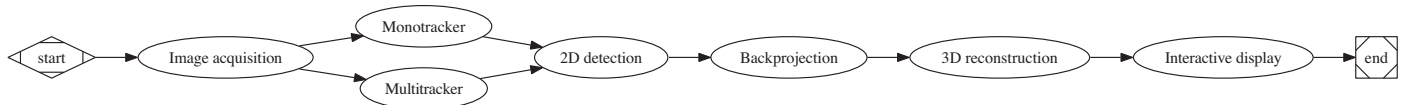
Fig. 2. The proposed real-time 3D position reconstruction method.

What is the influence of the discretization? We discuss the first issue here while (b) and (c) are discussed in Sections 3.5 and 3.4.1, respectively.

The reconstruction $\hat{f}$ must be located inside the restrictive volume and placed on a surface that is uniquely defined by g and by the perspective transform. The exact position of $\hat{f}$ on this surface may not be uniquely determined making $\hat{f}$ non-unique. Indeed, many reconstructions that meet all of the aforementioned criteria exist. To reduce the number of solutions some additional knowledge must be utilized. The allowed positions are already included via the restrictive volume, but the intrinsic properties of the guidewire are not included. We include these properties through a cost function that determines the quality of every possible $\hat{f}$. An optimization technique is used to reduce the number of solutions by selecting the ones having the best properties. The uniqueness of the reconstruction cannot again be guaranteed due to the existence of configurations where the solution is ambiguous even with the properly chosen cost function. Therefore all found solutions must be presented to the physician as the reconstruction ambiguity cannot be resolved.

3.3. 2D segmentation

Before discussing the proposed 3D reconstruction we give a brief overview of the processing tasks to find the 2D projection of the guidewire.

The important properties of the guidewire are: (a) it is an elongated structure and (b) it may move between two adjoint frames. Segmentation and tracking methods should take both into consideration. To simplify the design at least two distinct trackers are desirable, one for the spatial segmentation in a single frame and one for the temporal movement tracking in a sequence of frames. We refer to the first one as the *monotracker* and to the second one as the *multitracker*. Such a concept is modular and is also desirable for the implementation as separate 2D trackers makes overall design simpler while admitting parallel operation.

3.3.1. The monotracker

The primary purpose of the monotracker is spatial detection of elongated line-type structures. Various methods are used for enhancement and detection of line-type structures. For the guidewire segmentation the Marr-Hilderth-like filters are used in [23], while Baert et al. have experimented with the Hessian matrix-based method [3] and coherence-enhancing diffusion [36]. The Hessian matrix-based methods [3,13,27,17] are used most often, especially the vesselness measure introduced by Frangi et al. [13] that has been successfully used in medical imaging to enhance the line-type structures ranging from vessels to guidewires. We use a compensated vesselness map with automatically selected optimal parameters [25]. An example result is shown in Fig. 3(b).

3.3.2. The multitracker

The multitracker should combine both the temporal and the spatial information with the emphasis on the guidewire movement to complement the monotracker. The simplest technique is the subtraction of two adjoint frames, while better approaches use the background subtraction. Using subtraction for the X-ray modality is *incorrect* as the result is modulated by the image intensity due to a transitive nature of the imaging modality [14,24]. Additional problems also arise due increased noise after subtraction. We use a background estimation technique where the moving guidewire is detected by a background division that eliminates unwanted modulation and reduces noise [24]. An example result is shown in Fig. 3(c).

3.3.3. Combining 2D detection results

The monotracker and multitracker results must be combined together so that: (a) strong detections by either tracker still remain strong and (b) weak simultaneous detections by both trackers become stronger than weak detections by a single tracker. Due to the real-time constraints the results are merged using a boolean OR operation and multiple thresholds, two for each tracker. Higher thresholds $t_{H,\cdot}$ are used for thresholding the output of a single tracker and lower thresholds $t_{L,\cdot}$ are used for simultaneous thresholding of all outputs:

$$(\mathcal{V} > t_{H,\mathcal{V}}) \vee (\mathcal{T} > t_{H,\mathcal{T}}) \vee ((\mathcal{V} > t_{\mathcal{L},\mathcal{V}}) \wedge (\mathcal{T} > t_{\mathcal{L},\mathcal{T}})), \tag{1}$$

where $\mathcal{V}$ is the vesselness value (monotracker result), $\mathcal{T}$ is the estimated thickness (multitracker result, logarithm of the background division) and t denotes the corresponding threshold values.

The final result is an unstructured set of pixels with local line orientation [25] and estimated projected thickness [24] attached to
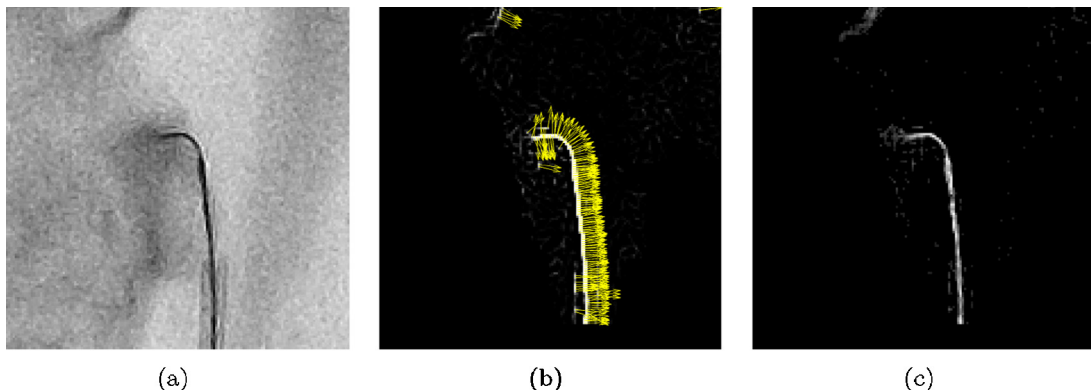

Fig. 3. Typical 2D detection results before thresholding: (a) input image, (b) monotracker result (vesselness map with eigenvectors orthogonal to local line orientation [25]), and (c) multitracker result (non-calibrated thickness estimation [24]).
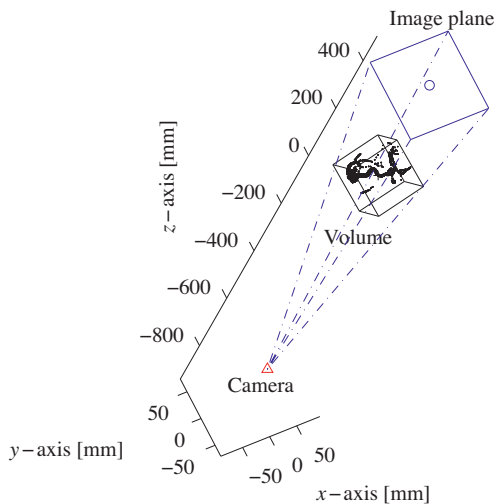
Fig. 4. The imaging geometry is defined by the positions of the camera (radiation source), of the image plane (flat panel detector) and of the restrictive volume (blood vessels).

each pixel. By not imposing the pixel ordering in 2D we delegate the problem into 3D where it can be solved in a more natural way. Note that ordering relation can be imposed as the detected pixels are on a 2D curve, however, this requires assumptions about the curve properties and is not trivial if the curve exhibits self-intersections or cusps.

3.4. Backprojection

Let us discuss the subproblem of reconstructing the surface that contains the guidewire. As stated in Section 3.2 the surface is uniquely defined by g and the perspective transform. This surface will be represented by a structured set of samples, either lines or points.

A monoplane C-arm imaging geometry shown in Fig. 4 is defined by: (1) the world position of the camera and (2) the world position and the number and dimensions of pixels of the image plane. Projection and back-projection are straightforward under known imaging geometry [12,35]. For the 3D reconstruction using a single view the world position and the number and dimensions of voxels of the restrictive volume must also be known. This is performed by registering the restrictive volume to the 2D image. The proposed method assumes that the perspective geometry is known, that the restrictive volume is registered to the X-ray image, and that the X-ray image is geometrically corrected for various distortions. Registration is performed as described in [29], and X-ray image is corrected as described in [29,9].

3.4.1. Sampled surface reconstruction

Let c be the camera focal point. The image plane P is defined by the central point p and the plane normal $\mathbf{n}_P$ in the direction

from p toward c. Let $\hat{g}(n) = (x_{n,2D}, y_{n,2D}) = a_{n,2D}$ be the nth found point in the unstructured set of 2D guidewire points (Section 3.3), so $a_{n,2D}$ denotes the nth selected pixel in the image plane. The imaging geometry then defines a corresponding 3D point $a_{n,3D} = (x_{n,3D}, y_{n,3D}, z_{n,3D})$ on P [12,35]. For each $a_{n,3D}$ we compute the finite line segment $L(a_{n,3D}, c)$.

Additional knowledge is provided by the restrictive volume. The basic elements of the restrictive volume are voxels. Only voxels corresponding to the blood vessels are considered. Each line $L(a_{n,3D}, c)$ is broken into disjoint segments $L(a, b)$, $a \neq b$, where a and b are intersection points between $L(a_{n,3D}, c)$ and sides of a voxel it intersects (Fig. 5). The set of all segments is an unstructured set whose elements can be interpreted as samples of the true backprojection surface if the points $\hat{g}(n)$ are error free. We call this set a sampled backprojection surface. The sampled backprojection surface can have a complex shape if the projected curve exhibits self-intersections or cusps.

3.4.2. Sampled surface topology

The 2D detection result and the sampled backprojection surface are unstructured sets. For visualization purposes this does not present a problem as a human observer will perceive the structure when the result is visualized. For the reconstruction task a structure that defines connectivity must be imposed on the sampled backprojection surface.

To impose some structure in a computationally efficient way we reuse a precomputed topology of the restrictive volume. The topology of the restrictive volume is summarized by its skeleton that captures the anatomy of the blood vessels making it suitable for the guidewire reconstruction tasks. The skeleton is computed by thinning and pruning on the preoperatively obtained volumetric data set. The skeleton is divided into branches with each branch having a total ordering and the whole skeleton having a partial ordering. This natural ordering is extended to all segments from the sampled backprojection surface by using proximity to the skeleton point as the extension criteria. The sampled backprojection surface inherits the topology and the structure of the vessel tree skeleton as shown in Fig. 7(b).

3.4.3. Precision and uncertainty

The reconstruction precision is limited by the maximum sampling distance on the sampled backprojection surface, which depends on the image and volume resolutions. For the guidewire reconstruction the region of interest is located between the imaging plane and the camera focal point (Figs. 4 and 5).

The image resolution is limited by the detector sampling grid. If the pixels are rectangles with the diagonal l_1 then the worst resolution is l_1. The restrictive volume voxels are sampled from the underlying continuous volume, e.g. segmented vessels are obtained from the resolution limited volumetric data. If the voxels are rectangular cuboids with the largest diagonal l_2 then the worst resolution is l_2. The reconstruction precision cannot be better than the maximum of l_1 and l_2.
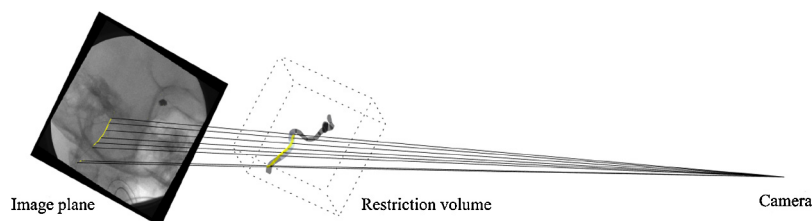

Fig. 5. Backprojection. To reconstruct the 3D position of the guidewire we trace a line between 2D position and the camera position. Intersections between traced lines and segmented vessels are possible 3D positions.
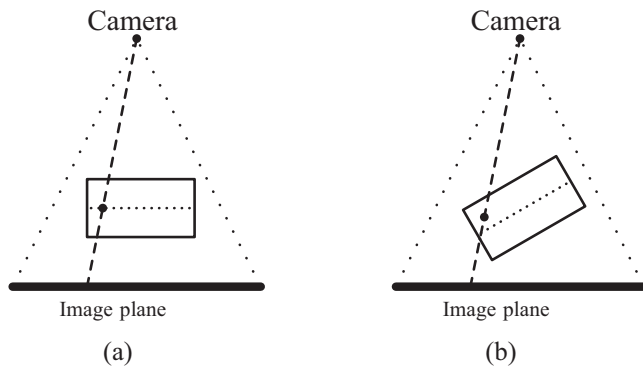
Fig. 6. Collapsing segments to point representatives. For a long tubular vessel a representative point will be centered regardless of its position (a). Positions near the vessel endpoints will be moved away from the true centerline (b).

The restrictive volume is composed of voxels so one backprojection line $L(a_{n,3D}, c)$ is split into multiple subsegments $L(a, b)$. Under the assumption of a single guidewire per vessel the adjoining line subsegments can be collapsed into a single representative central point (Fig. 6(a)). Such data reduction simplifies the reconstruction. To avoid the unwanted data loss in addition to the central point both direction and length of each segment is stored as they represent the position uncertainty.

In real world applications, the imaging model and the restrictive volume are not ideal so we must compensate for errors. The main sources of error are registration errors and vessel wall movements during the procedure making the guidewire appear to be outside of the vessels. In order to compensate for this effect we dilate the restrictive volume. The dilation makes the reconstruction possible in the presence of errors at the cost of increased uncertainty and decreased precision in the 3D position that are proportional to the amount of the dilation. A dilated restrictive volume example is shown in Fig. 7(a).

The collapse of the line subsegments can cause a reconstruction bias. Whenever the line subsegments are close to the object boundary the bias can manifest as a movement of the representative point away from the true object centerline (Fig. 6(b)). The effect is noticeable at the ends of the vessel segment and when dilation does not produce a symmetrical extension due to neighboring vessels. A large variety of possible shapes makes this bias difficult to remove.

3.5. Guidewire reconstruction

The structured set of lines (or points) representing the sampled backprojection surface is the unique solution to the reconstruction problem (Fig. 7). Any curve on this set can represent the guidewire. To resolve the ambiguity a single curve should be selected. Selecting

a single curve is not always possible so all viable curves that satisfy certain properties should be identified and presented as the solution. The proposed method selects a single curve and, due to real-time computational constraints, partially identifies and presents a subset of all viable curves.

In the proposed method, we use a local greedy optimization approach to the guidewire position reconstruction problem that finds a curve on the sampled backprojection surface that is an approximate local minimizer for some predetermined cost function. However, a non-greedy optimization method could also be used as evident from a vast literature on the topic [22]. The proposed cost function is expressed as a linear combination of the position dependent factors that take into consideration both the position on the structured set and the local position on the curve itself. The cost function factors corresponding to the local curve position are intended to encode the knowledge about the guidewire. The terms dependent on the position on the sampled surface are intended to encode the anatomical knowledge.

An important property of any optimization approach is the required computational time. The size of the search space is prohibitively large and optimization via exhaustive search does not allow real-time operation. This limitation can be overcome by a customized design of the optimization procedure that is able to find approximate solutions of sufficient quality.

3.5.1. Reconstruction ambiguity and critical points

The set of samples forming a sampled backprojection surface will not be simply connected due to the self-intersections and cusps in the 2D guidewire projection and due to the complex anatomy of the blood vessels. This complex shape of the sampled backprojection surface makes the reconstruction by greedy optimization locally unstable.

Under the assumption of a single guidewire the reconstruction ambiguities arise due to (a) self-intersections and cusps of the 2D projection and due to (b) vessel tree branching points. Both are critical as for every ambiguity, either a self-intersection or branching, there exists a set of distinct extrema of the cost function that a naive greedy optimization cannot capture. To stabilize the proposed greedy scheme all critical points must be identified before the optimization starts and must be used to guide the optimization.

The critical points due to the complex blood vessel anatomy are identified as the branching points of the topological skeleton. On-the-fly computation of the skeleton of the sampled backprojection surface for every frame is computationally expensive so a skeleton of the restrictive volume is used as a reasonable approximation (Section 3.4.2). Every skeleton branching point induces a possible split in the reconstruction, e.g. n connected branches introduce an n-way split. For every split all possible paths must be examined. This is achieved by guiding the greedy optimization to select a local candidate for every of $n - 1$ possible branching directions. An
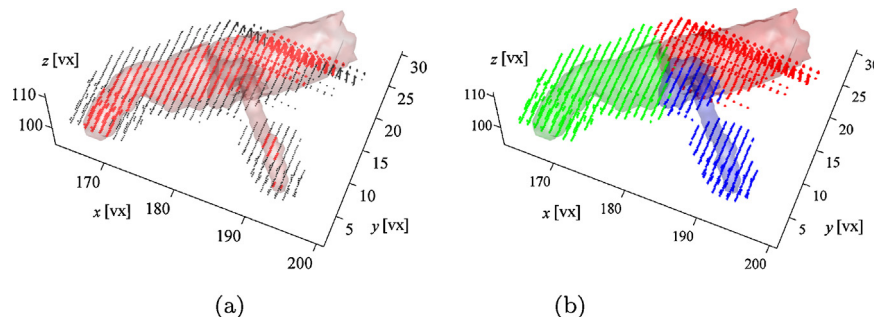

Fig. 7. A sampled back-projection surface showing one larger vessel with a smaller vessel branching down: (a) shows extension of the surface to allow for errors (Section 3.4.3) and (b) shows the partition induced by the skeleton of the restrictive volume.
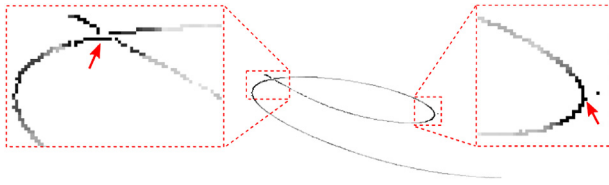
Fig. 8. Spreads (standard deviations) of the local angle histogram for 9×9 neighborhoods. Self-intersections and cusps have larger spreads. Local extrema are selected as the splitting points. For selected splitting points disjoint histogram modes define major directions.

example partition of the sampled backprojection surface induced by a three-way branching point is shown in Fig. 7(b).

The critical points that arise due to cusps and self-intersections are found in the monotracker result (Section 3.3.1) by testing the distribution of local line orientations for unimodality—if the distribution is multi-modal with n modes then it introduces an n-way split. Due to a small histogram size and real-time constraints we cannot use standard unimodality/multimodality tests, e.g. [28,21]. Instead we use fixed 12 bin histogram and 9×9 neighborhoods. From the 9×9 neighborhood only curve points connected to the central point are taken into consideration. Connections are determined by analysis of the extracted line directions as proposed in [31]. If there is at least one bin separation between the mode and the second largest histogram count the point is identified as the critical point. Then all histogram modes having more than three members are considered to be separate directions. The three point limit is chosen to allow for locally sharp bends. A limited non-maximum suppression is achieved by taking into consideration only those points where the local angle spread (deviation) is the local extrema (Fig. 8).

3.5.2. A fast iterative greedy optimization method

The greedy reconstruction must find near-optimal curves with regard to some chosen cost function. The basic iteration step consists of picking the best possible continuation point and adding it to the curve. The added point becomes a new endpoint and the process is repeated.

The cost function must satisfy the following desirable properties: (1) Picking the central position for each ray minimizes the worst case reconstruction error to half the local intersection thickness. The cost function should favor central positions. (2) Additional properties of the guidewire, such as local curvature or bending constraints, must be incorporated into the cost function. (3) When iteratively constructing the curve the process of picking the starting point, the second point (and thus the starting segment), and consecutive points is different and each requires a subtly adjusted cost function. At least two points are needed to find the line orientation and at least three are needed for curvature making the cost function different based on the number of accumulated points in the reconstruction. (4) The cost function must be aware of the spatial sampling and of the locally varying resolutions of the backprojection surface. Any cost function that satisfies the above mentioned properties can be used in an iterative greedy curve reconstruction scheme.

There are two significant problems that must be addressed to make the proposed scheme robust: (a) how to reliably choose the starting segment and (b) how to augment the greedy scheme so it does not fail in the case of multiple local optima. The first problem is solved by selecting the appropriate cost function factors (Section 3.5.3) and by requiring a simultaneous choice of the first point pair that forms a starting segment. To solve the second problem a set of critical points where multiple local extrema exist must be identified. The first two classes of critical points are the self-intersections and cusps of the projection and the branching points of the vessel

tree (Section 3.5.1). A third class of critical points is introduced by the properties of the chosen cost function and for the proposed cost function the critical points are introduced during selection of the starting segments.

3.5.3. Cost function factors

For simplicity, we propose a cost function that is a linear combination of factors. Some of the factors are inspired by the equations used for the guidewire propagation simulation described in [1].

Let a and b be the two last points from the curve forming an end segment and let c be the next candidate point to be added. Once c is added the point sequence is a, b, c making c the new endpoint and making bc the new end segment. Let $\mathbf{v}_{ab}$ be a vector from a to b and let $\mathbf{v}_{bc}$ be a vector from b to c. Let m_c be the closest skeleton centerline point to c, let $\mathbf{n}_c$ be a vector showing preferred local line direction (vessel cross-section normal), and let $\mathbf{i}_c$ be a local 2D line orientation vector (result of the Hessian matrix eigenanalysis). Subscript 2D denotes projected coordinates or direction vectors.

The factors of the cost function that are tied to the dataset representing the sampled backprojection surface are:

1 Squared distance to the closest centerline point to favor central positions: $d^2_{\mathrm{3D}}(c, m_c) = ||c - m_c||^2_2$.
2 Local 3D line orientation cost to favor alignment with the vessel direction:

$$o_{\mathrm{3D}}(\mathbf{v}_{bc}, \mathbf{n}_c) = \arccos^2 \frac{\mathbf{v}_{bc} \cdot \mathbf{n}_c}{||\mathbf{v}_{bc}|| \, ||\mathbf{n}_c||}.$$

3 Local 2D line orientation cost to favor alignment with the detected 2D line direction:

$$o_{\mathrm{2D}}(\mathbf{v}_{bc,\mathrm{2D}}, \mathbf{i}_b) = \arccos^2 \frac{\mathbf{v}_{bc} \cdot \mathbf{i}_b}{||\mathbf{v}_{bc}|| \, ||\mathbf{i}_b||}.$$

We use the local 2D direction at point b as this direction is relevant when moving to point c.
4 Deformation cost that is proportional to the squared displacement of the point c outside of the non-dilated restrictive volume. If we assume round vessels with local radius r_c for the point c then the cost term is $(d_{\mathrm{3D}}(c, m_c) - r_c)^2_+$.

The factors of the cost function tied to the local position on the curve are:

1 Squared distance to the next candidate point $d^2_{\mathrm{3D}}(c, b) = ||c - b||^2_2$. This factor limits the search area to the points close to the curve endpoint.
2 Projected distance to the next candidate point $d^2_{\mathrm{2D}}(c, b) = ||c_{\mathrm{2D}} - b_{\mathrm{2D}}||^2_2$.
3 Bending energy in 3D computed from the radius of the osculating circle [5] as

$$\kappa^2_{\mathrm{3D}} = \frac{2(d^2_{ab}d^2_{bc} + d^2_{bc}d^2_{ca} + d^2_{ca}d^2_{ab}) - d^4_{ab} - d^4_{bc} - d^4_{ca}}{d^2_{ab}d^2_{bc}d^2_{ca}},$$

where d_{ab} is length of the vector from a to b etc.
4 Bending energy in 2D computed from the radius of the osculating circle as in previous factor, but with projected distances instead of 3D distances; replace d_{ab} with $d_{ad,\mathrm{2D}}$, etc.
5 Approximation to 3D flexural rigidity [1]

$$D_{\mathrm{3D}} = \arccos^2 \frac{\mathbf{v}_{ab} \cdot \mathbf{v}_{bc}}{||\mathbf{v}_{ab}|| \, ||\mathbf{v}_{bc}||}.$$

6 Approximation to 2D flexural rigidity

$$D_{2D} = \arccos^2 \frac{\mathbf{v}_{ab,2D} \cdot \mathbf{v}_{bc,2D}}{||\mathbf{v}_{ab,2D}|| \, ||\mathbf{v}_{bc,2D}||}.$$

7 Dot products between vectors $\mathbf{v}_{ab}$ and $\mathbf{v}_{bc}$ and projected vectors $\mathbf{v}_{ab,2D}$ and $\mathbf{v}_{bc,2D}$ that are only examined to limit the search area to forward motion thus preventing curve back-flips.

The total cost is computed as a weighted combination of the above mentioned factors. The factors can be grouped together for easier interpretation to form the knowledge part

$$C_M = \alpha_M d_{3D}^2(c, m_c) + \beta_M o_{3D}(\mathbf{v}_{bc}, \mathbf{n}_c) + \gamma_M o_{2D}(\mathbf{v}_{bc}, \mathbf{i}_b)$$
$$+ \delta_M (d_{3D}(c, m_c) - r_c)_+^2, \tag{2}$$

the 3D part

$$C_{3D} = \alpha_{3D} d_{3D}^2(c, b) + \beta_{3D} \kappa_{3D}^2 + \gamma_{3D} D_{3D}, \tag{3}$$

and the 2D part

$$C_{2D} = \alpha_{2D} d_{2D}^2(c, b) + \beta_{2D} \kappa_{2D}^2 + \gamma_{2D} D_{2D}. \tag{4}$$

The total cost is a sum of (2), (3) and (4)

$$C = C_M + \alpha C_{3D} + (1 - \alpha) C_{2D}, \tag{5}$$

where the superficial term α was added to enable simpler global control of the weight ratio between the symmetrical parts C_{3D} and C_{2D} that determines if 2D or 3D part of the cost function is more valued.

The absolute values of most of the weighting factors are not relevant for the local greedy minimization making the choice of parameters flexible. It is sufficient to specify relative values of the factors and then choose the scale to obtain the sufficient numerical precision. Nevertheless, it is important to place more weight to the stable cost function factors. The stable factors are the ones forcing the curve to match the data we trust. This data are the 2D position, the 2D line orientation, and the vessel centerline position; thus α_M and γ_M must be significantly larger than other parameters. For C_{3D} and C_{2D} we should place more trust into the 2D part as it is image guided. We found that a large β_M introduces problems due to limits in the estimation of the $\mathbf{n}_c$ while large values of γ_{3D} and γ_{2D} tend to locally force the solution to form short straight segments that can result in a zig-zag curve that deflects from the vessel walls. Sufficiently large α_M and γ_M together with smaller α_{3D} and α_{2D} and with other parameters significantly smaller produce a stable reconstruction that does not depend on the absolute parameter values. A centerline reconstruction as proposed by van Walsum et al. [33] can be achieved by setting all parameters except α_M and γ_M to zero with the additional advantage of skipping the 2D curve parametrization step.

The cost (5) is evaluated only if the candidate point is within the valid search area. The search area is determined from the distances $d_{3D}^2(c, b)$, $d_{2D}^2(c, b)$ and dot-products; we extend the curve forward as far away as the local vessel thickness. Furthermore, the cost function terms are evaluated in order of the increasing computational complexity to reduce the computational cost by an early rejection of points with prohibitive cost.

It is important to correctly select the starting segment as it defines how the reconstruction behaves. Due to a limited computational time we cannot examine reconstructions for each of the possible starting segments. Furthermore, the cost function used for selecting the starting point pair must be modified as both bending energy and flexural rigidity cannot be computed. Per requirements (Section 3.5.2) and to make the choice stable we construct the cost function so the non-isolated points having a strong 2D detection
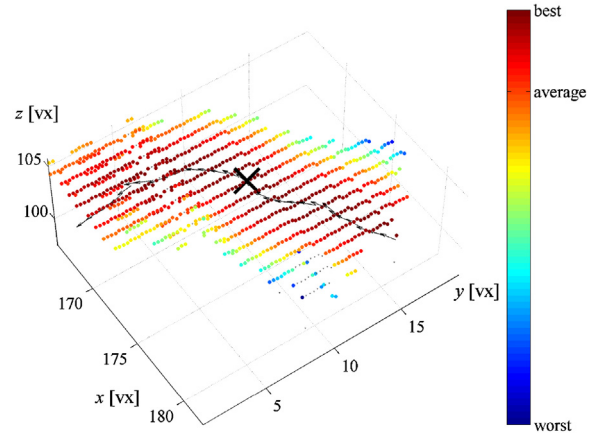

Fig. 9. The costs for the first point for 2D detection results in Fig. 3. The chosen point is marked by X. The skeleton centerline is shown as a black path.

that are far from the critical points are preferred. The cost function for the first point of the starting pair is

$$C_1 = \alpha_1 d_{3D}^2(a, m_a) + \beta_1 \left(\frac{1}{2} - r(a)\right)^2 + \gamma_1 \mathcal{V} + \delta_2 (d_{3D}(a, m_a) - r_a)_+^2, \tag{6}$$

where $\mathcal{V}$ is the vesselness value and $r(a) \in [0, (0.5)]$ is the relative distance to the closest vessel tree branching point measured along the centerline from the closest centerline point m_a. For the second point the cost function includes parts of (5) that can be computed given only two points excluding term $(0.5) - r(a)$ from (6),

$$C_2 = \alpha_2 d_{3D}^2(b, m_b) + \beta_2 o(\mathbf{v}_{ab}, \mathbf{n}_b) + \gamma_2 o(\mathbf{v}_{ab}, \mathbf{i}_a)$$
$$+ \delta_2 (d_{3D}(b, m_b) - r_b)_+^2 + \epsilon_2 d_{3D}^2(a, b) + \zeta_2 d_{2D}^2(a, b). \tag{7}$$

For the starting segment we pick the starting point pair that has the lowest overall cost $C_1 + C_2$. The same arguments valid for choosing parameters for (5) apply.

The sampled cost function values for the first point are shown in Fig. 9. We favor points closer to the centerline and to the branch center. The sampled cost function values for the second point are shown in Fig. 10. The cost function is symmetrical so the curve can extend on both sides making the starting segment a critical point introduced by the cost function (Section 3.5.1). The starting segment can be placed anywhere on the true guidewire so both alternatives must be examined. Fig. 11 shows the sampled cost function for a point on the curve having more than two points. The
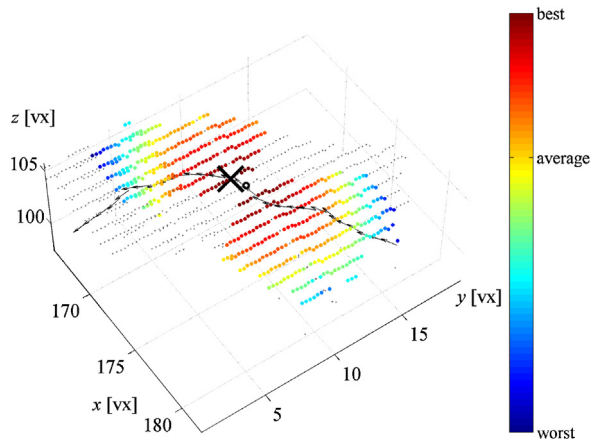

Fig. 10. The costs for the second point for 2D detection results from Fig. 3. The chosen point is marked by X. The skeleton centerline is shown as a black path.
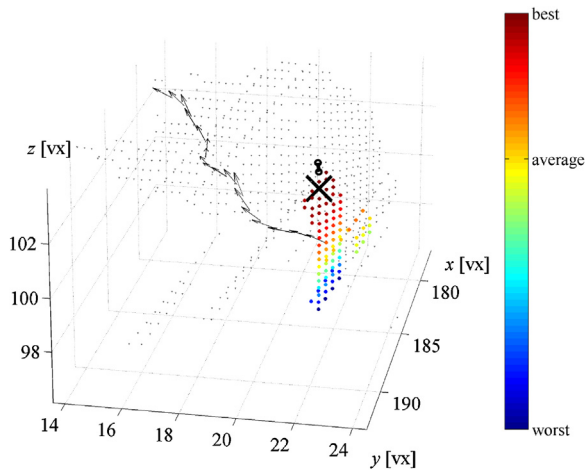
Fig. 11. The costs for adding the next point to the curve for 2D detection results from Fig. 3. The chosen point is marked by X. The skeleton centerline is shown as a black path.

optimal value of the cost function is always forward of the ending segment (back-flips are prohibited).

3.5.4. Parallel curve reconstruction

The cost function of Section 3.5.3 is used in an iterative greedy optimization scheme where the curve is started and extended until all 2D points are covered.

The developed software implementation is parallel and requires a priority queue, a dispatcher thread and as many worker threads as possible. The queue element stores information about the curve segments and about the region of interest (ROI). The reconstruction starts by pushing all disjoint areas of the restrictive volume into the queue. The dispatcher then assigns elements from the queue to worker threads. Each worker thread behaves as follows (Fig. 12):

1 Wait for the next element from the processing queue.
2 Check if there is a curve end segment in the element's ROI.
3 If there is no curve try to start one in the element's ROI by optimizing the sum of costs (6) and (7).
4 If a suitable starting segment is found push it twice into the queue with two possible propagation directions. Go to step 1.
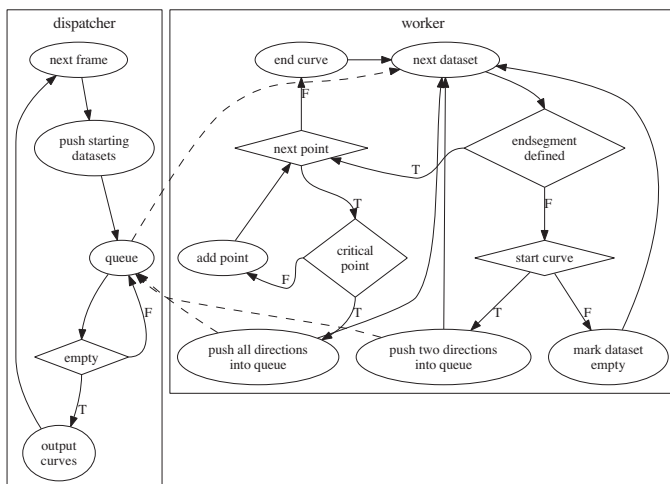5 If there is a curve try to find the next point with minimal cost (5). If there is none go to step 1.

Fig. 12. The parallel curve reconstruction using the proposed greedy optimization scheme.
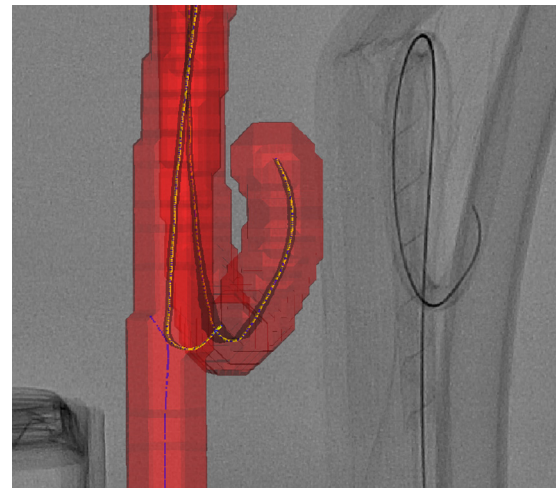

Fig. 13. Instability of the local optimization scheme. Once a critical point (here a self-intersection) is reached the guidewire can continue either way. Two of several possible solutions are shown. The volume and 2D image are misaligned to make self-intersection in 2D visible.

6 If the point is not in the proximity of a critical point add it to the curve. Go to step 5.
7 If the point is in the proximity of a critical point identify all possible directions and corresponding ROIs and push them into the queue. Go to step 1.

Besides the task assignment the dispatcher tracks the state of all curve segments together with the total cost for each of the found curves. Once this process completes all found curves are sorted based on the total cost and the curve having the farthest distal tip is selected as the primary reconstruction. For the interactive display all found curves are displayed and selected one is highlighted.

The computational time of 12 fps is chosen as a trade-off between the minimum frame rate required for motion perception and the radiation dose. The parallel reconstruction can terminate while there are unprocessed elements in the queue. To make the effects of dropping unprocessed elements insignificant a breadth first search approach is used by assigning appropriate priorities to the segments in the processing queue.

The stabilizing step for the proposed greedy optimization scheme is the splitting step at the critical points. This is essential as there is no *stable* local optimization method that can guarantee both robust and correct curve continuation. With the splitting step missing the cost function can guide the curve either way (Fig. 13).

3.5.5. Spline smoothing

The reconstruction result is an ordered set of 3D points that do not always form a completely smooth curve. Sharp bends in the reconstruction are usually situated at the splitting points where we locally force the reconstruction into many different paths. To produce a smooth reconstruction and to interpolate between points for display purposes a smoothing natural cubic spline with arc-length parametrization [8] is used.

4. Experiments

The described 3D guidewire reconstruction method was quantitatively evaluated on five phantom datasets and was qualitatively evaluated on two patient datasets. All datasets were acquired using the Philips Allura C-arm X-ray imaging system. A built-in state of the art distortion correction and volume-image registration were used [29].

Table 1
Phantom acquisitions

No.	Volume		Image		
	Voxel	Size	Frames	Pixel	Size
1	0.573 mm	256^3	12	0.217 mm	1016^2
2	0.410 mm	256^3	21	0.217 mm	1016^2
3	0.573 mm	256^3	9	0.217 mm	1016^2
4	0.573 mm	256^3	16	0.217 mm	1016^2
5a	0.410 mm	256^3	6	0.217 mm	1016^2
5b	0.410 mm	256^3	7	0.154 mm	864^2

The parameters were the same for all performed experiments. The parameters for the 2D detection were automatically set as described in [24,25]. The thresholds for (1) were set to $t_{H,\mathcal{V}} = 0.4$, $t_{L,\mathcal{V}} = 0.35$, $t_{H,\mathcal{T}} = 0.4$ and $t_{L,\mathcal{T}} = 0.35$. The local angle histograms of Section 3.5.1 were computed from the 9×9 neighborhood with fixed 12 bins. The parameters for the cost function (5) were $\alpha_M = 4$, $\beta_M = (0.125)$, $\gamma_M = 32$, $\delta_M = 128$ (to clearly separate dilated area), $\alpha_{3D} = 1$, $\beta_{3D} = 2$, $\gamma_{3D} = (0.25)$, $\alpha_{2D} = 32$, $\beta_{2D} = 4$, $\gamma_{2D} = (0.5)$ with $\alpha = (0.5)$ so both (4) and (3) are equally favored. The parameters for (6) and (7) were $\alpha_1 = 4$, $\beta_1 = 1$, $\gamma_1 = 1$, $\delta_1 = 128$ and $\alpha_2 = 4$, $\beta_2 = 1$, $\gamma_2 = 1$, $\delta_2 = 128$, $\epsilon_2 = 4$, $\zeta_2 = 4$. For the cubic spline of Section 3.5.5 weight for the interpolation term is set to $\mu = 0.15$ ($\lambda = 2(1 - \mu)/(3\mu) = 3.78$), and the weight for the energy of the second derivative is $1 - \mu$. These parameter values have produced very good results. However, the selection of the optimal parameters is an open topic for future research.

4.1. Phantom acquisitions

The image acquisitions for each of the stationary guidewire phantoms were performed with the acquisition parameters listed in Table 1. All volumes were reconstructed from 120 images spanning $240°$ using 83 kV and 153 mA. All 2D images were acquired using 80 kV and 20.1 mA. All voxel are cubes and all pixels are squares. The C-arm position (viewpoint) for every acquired frame was different.

For the phantom datasets the true 3D position of the guidewire was obtained by the Philips 3D-RA/XperCT software using the cone-beam reconstruction method. The cone-beam reconstruction of the guidewire was locally 3–5 voxels thick due to partial volume effects. The centerline of this reconstruction is considered to be the ground truth. The restrictive volume was obtained from the reconstructed tubing that was holding the guidewire in place, except for the second phantom where the restrictive volume was obtained by dilation of the cone-beam reconstruction.

The phantom datasets were selected to test configurations of interest for the 3D reconstruction from a single 2D image. The first phantom case contains a single guidewire making a full circular loop in 3D that crosses itself in some of the projections, depending on the view direction (Fig. 14(a)). The rotation of the C-arm to obtain different views was around the principal axis of the wire. The loop formed by the guidewire is large compared to the image resolution. The second phantom case contains a single guidewire that crosses itself once in the projection (Fig. 14(b)). The loop in the middle of the guidewire is small compared to the image resolution. The third phantom case is similar to the first one except the guidewire makes half of a circular loop in 3D (Fig. 14(c)). The fourth phantom case contains one single straight guidewire with the J shaped tip (Fig. 14(d)). The fifth phantom case contains one single wire that does not cross itself in the projections (Fig. 14(e)).

Fig. 15

4.2. Patient datasets

Two recordings made in the clinic during neuro-endovascular interventions were used. For both datasets immediately prior to the intervention a 3D scan using a contrast medium and the same C-arm device was performed. From this scan both vessel segmentation and the vessel skeleton were obtained.

5. Results and discussion

To evaluate the reconstruction the distance between two curves must be measured. A good distance measure is the Hausdorff distance [10,19]. If X and Y are two sets in $\mathbb{R}^n$ and if x and y denote elements from X and Y, respectively then Hausdorff distance is

$$d_H(X, Y) = \max\{\underbrace{\sup_x \inf_y d(x, y)}_{d_{H,xy}}, \underbrace{\sup_y \inf_x d(x, y)}_{d_{H,yx}}\} \qquad (8)$$

where d is a distance function on $\mathbb{R}^n$. Although the Hausdorff distance provides a good error measure it is sensitive to outliers. To compensate for outliers the distances are averaged [10,2],

$$d_{MH}(X, Y) = \frac{1}{2}\underbrace{\text{mean}_x \inf_y d(x, y)}_{d_{MH,xy}} + \frac{1}{2}\underbrace{\text{mean}_y \inf_x d(x, y)}_{d_{MH,yx}}. \qquad (9)$$

The term $\text{mean}_x \inf_y d(x, y)$ can be interpreted as the average distance one must travel to align X with Y.

5.1. Phantom acquisitions

For phantom acquisitions the guidewire was stationary. The movement of the guidewire is not relevant for the evaluation as the proposed method uses a single 2D frame for the 3D reconstruction. In practice the allowed movement is constrained by the image acquisition process as there must be no motion artifacts.

Table 2 lists the measured distances between the cone-beam reconstruction (X) and the proposed reconstruction (Y). Due to
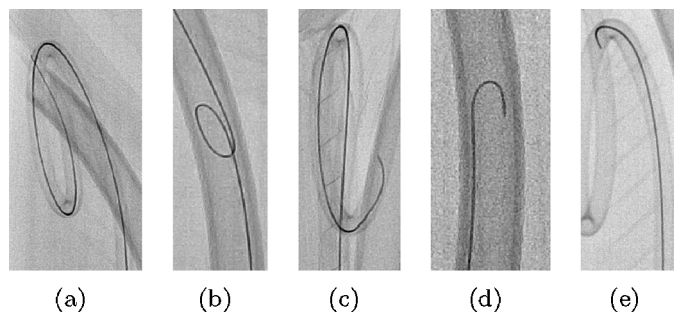

(a)　　　(b)　　　(c)　　　(d)　　　(e)

Fig. 14. Representative X-ray images for five phantoms.

Table 2
Total reconstruction errors. Hausdorff (8) and modified Hausdorff (9) distances are measured in voxels. Sample mean and sample standard deviation are given both with and without (w) outliers. Outliers were removed manually.

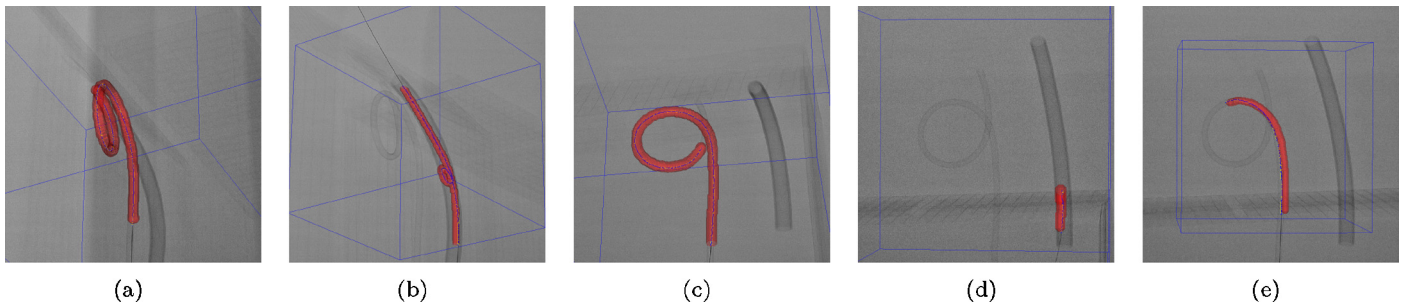| Case	Frames	d_H	$d_{H,xy}$	$d_{H,yx}$	d_{MH}	$d_{MH,xy}$	$d_{MH,yx}$
1	12 (2)	11.87	8.84	7.59	1.13	1.35	0.90
2	21 (1)	6.68	5.15	5.81	1.73	1.72	1.74
3	9 (1)	8.84	6.68	4.71	1.16	1.55	0.77
4	16 (1)	9.91	7.52	6.76	2.63	3.09	2.16
5a	6 (0)	9.58	7.82	7.46	3.97	4.03	3.90
5b	7 (2)	35.67	34.96	5.15	8.37	14.57	2.17
Mean		11.67	9.67	6.26	2.60	3.41	1.79
Deviation		21.13	21.65	1.60	5.01	9.77	0.93
Mean (w)		7.92	5.75	6.36	1.87	1.96	1.78
Deviation (w)		4.54	5.25	1.50	1.04	9.77	0.93

Fig. 15. Restrictive volumes for five phantom datasets. Note the registration error for (e).

auto-adjustment of the acquisition system several input frames were either under or overexposed making the reconstruction fail due to poor 2D detection (number of failures is listed in parenthesis). Those frames were considered to be outliers. The average d_H for all datasets is about 11.67 vx (6.69 mm for largest voxel size, see Table 1) and this value can be taken as the average upper bound on the reconstruction accuracy. As there is no special treatment of the guidewire endpoints this is also the expected upper error for the tip. The average displacement is about 1.79 vx (1.02 mm). Overall, the maximal deformation distance is comparable to the vessel radius, as expected, since the reconstruction is resolution limited in the depth direction [33].

Comparison with the results from [33,2] shows the errors are comparable. In [33] about 2.31 mm mean distance and 3.58 mm for tip distance using manual 2D segmentation and monoplane reconstruction is reported. In [2] about 3.92 mm mean distance and 4.34 mm for tip distance using biplane reconstruction is reported. In our opinion for the proposed algorithm the errors are somewhat larger due to the reconstruction being fully automatic without any user intervention whatsoever. Furthermore, the method was constructed to work in real time making trade-offs unavoidable.

Two visualization examples are shown in Fig. 16. The reconstruction uncertainty is visualized as a semi-transparent surface around the guidewire. Such visualization is appropriate if pixels have significantly smaller dimensions than voxels so the dominant error is in the depth direction. It is especially important if the proposed method is used for navigation as it indicates the direction of the largest reconstruction error. A strong directionality of the error can be clearly seen in Fig. 16(b) at the top and the bottom parts of the circle the guidewire makes.

Fig. 17(a) shows the reconstruction for the second phantom (Fig. 14(b)) where the blood vessels are touching. This introduces difficulties as there are unneeded critical points introduced by the incorrect skeleton. The reconstruction depends on the correct skeletonization result and on the size of the search space for the
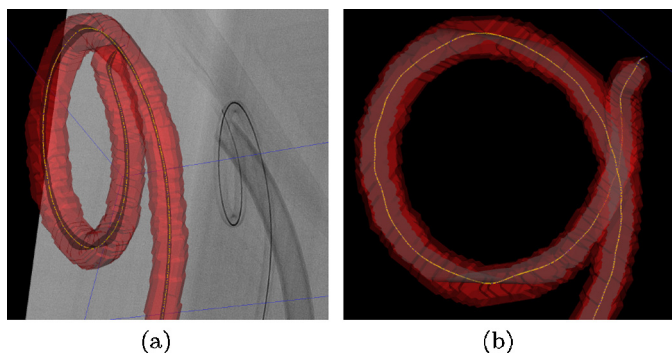
optimization making the true reconstruction difficult to achieve under limited processing time; automatically selected reconstruction for Fig. 17(a) is one that bypasses the loop entirely, while the alternate solution includes the loop. Fig. 17(c) and (d) demonstrates how the reconstruction for the J-shaped tip behaves depending on the view direction; reconstruction is impossible if the tip is oriented in the depth direction (Fig. 17(c)). Finally, Fig. 16(b) shows the correct reconstruction that is displaced due to registration errors. As the presented method is intended to be fully automatic this error was not corrected for so it affects the quantitative results.

5.2. Patient datasets

The proposed method is qualitatively evaluated on two patient datasets (Fig. 18). For these only a manual visual inspection of the results was possible as the ground truth cannot be established. Visual inspection established that the reconstructed guidewire always matches its 2D projection and is located within the vessels. The maximal reconstruction error is therefore not larger than the local vessel diameter.
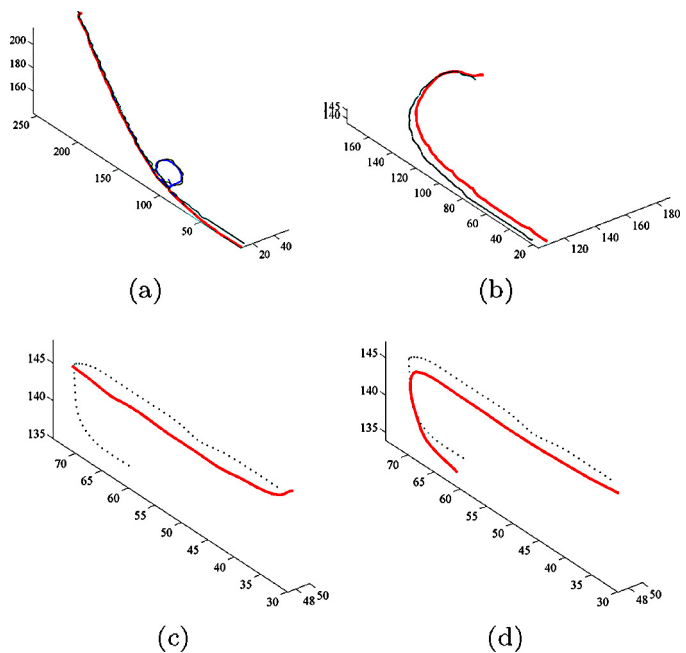

(a)   (b)

(c)   (d)

Fig. 17. Selected reconstructions shown in 3D. The dotted line is a cone-beam reconstruction and the full line is the proposed reconstruction: (a) shows the problem with the small loop in the middle of the guidewire, (b) shows the correct reconstruction for the fifth phantom with misalignment due to mis-registration, (c) shows the reconstruction where the J tip plane is parallel to the view direction for the fourth phantom, and (d) shows reconstruction where the J tip plane is orthogonal to the view direction for the fourth phantom.
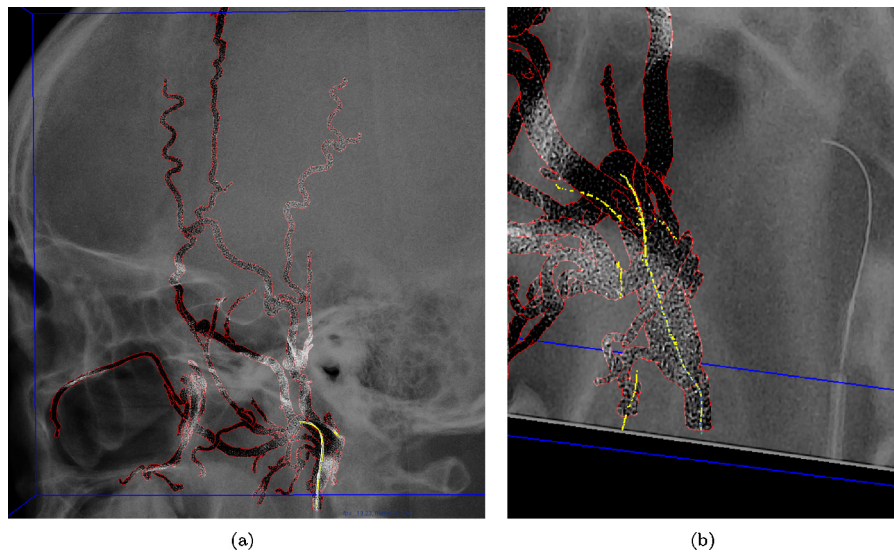

(a)   (b)

Fig. 16. Reconstruction uncertainties for two different views for the first phantom visualized as semi-transparent surfaces.

Fig. 18. An example reconstruction for a patient case: (a) the 3D reconstruction of the guidewire overlaid over the X-ray image and (b) a 3D view where all possible curve reconstructions are visible.

For some frames the reconstruction algorithm was unable to find a single continuous curve segment that represents the entire guidewire. The reconstruction was instead broken into segments at critical points, however, when all reconstructed segments are considered they fully cover the 2D projection.

5.3. Real-time operation

The proposed method was implemented in C++ using Intel IPP [15] and Intel MKL [16] libraries. Implementation was timed on Intel® Core™ i7 CPU 920 at 2.67 GHz. Table 3 shows execution times for the patient datasets (Section 4.2). The developed implementation achieves frame rate of 12 fps. Required memory is about 700 MiB (both phantom and patient cases).

5.4. Discussion

The effect of 2D segmentation on 3D reconstruction is determined by the quality of the chosen segmentation methods. Both selected methods are performing well within specified time constraints, are producing segmentations of sufficient quality and are auto-configurable without requiring user intervention [25,24]. As the proposed method does not require any additional processing to find semantic curve description in 2D there are no speed/accuracy trade-offs for the 2D processing.

Considering the proposed greedy reconstruction there are several speed/accuracy trade-offs as a brute-force search for the optimal solution is not feasible. Those are tied with the breath and depth of the search for the optimal solution, with the cost function parameters and with any possible post-processing steps to improve the solution.

The breadth/depth of the search had to be limited so the cost function is only evaluated for small set of proximal points. Given the real-time processing constraints the search must be terminated once the time limit is reached. Used search strategy is breadth first where elements in the priority queue (Section 3.5.4) are ordered so the first processing of any branch has higher priority then any subsequent processing. This ensures the whole vessel tree is examined at least once and postpones the search for alternate solutions caused by the critical points.

A reliable identification of critical points is crucial as it stabilizes the greedy optimization. For the vessel branching points the identification depends on the quality of the preoperatively obtained volume. For the guidewire induced critical points the identification depends on the quality of the cusp/self-intersections detector. However, even if both are near-optimal there are again configurations where the critical points cannot be identified from the data. Examples are the second phantom (Fig. 14(d)) where the touching vessels make the skeletonization find two non-existent branching points, and the fourth phantom (Fig. 14(d)) where different views of the J-shaped tip were acquired. For the J-shaped tip the correct reconstruction was achieved only when the imaging plane and the plane spanned by the J tip are (mostly) parallel making the J shape clearly visible (Fig. 17). This problem can be generalized—the

Table 3
Averaged cumulative computational times for the proposed method. Times are in milliseconds: t_1 includes data fetch, t_2 2D processing, t_3 back-projection, t_4 3D reconstruction, and t_5 smoothing and display. The sequence A has 496 frames of 1024^2 pixels and the volume of 256^3 voxels. The sequence B has 1407 frames of 1016^2 pixels and the volume of 256^3 voxels.

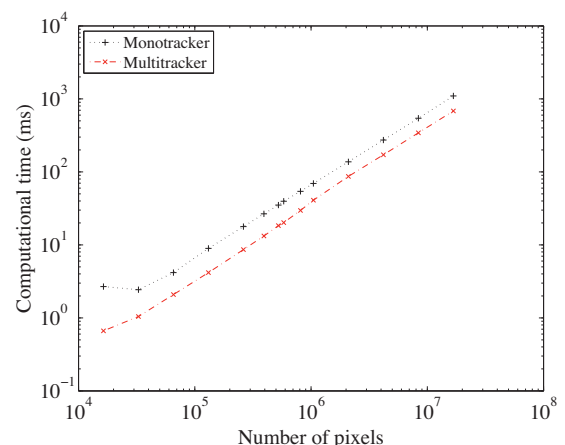| Sequence	t_1	t_2	t_3	t_4	t_5 (total)
A	2.21	45.21	67.70	76.27	81.74
B	1.41	32.24	51.37	66.49	70.03

Fig. 19. Image processing times vs. input image pixel count.

method cannot reliably recover curve features in the depth direction if the size of the feature is comparable to the local restrictive volume thickness.

Future possible research topics include adaptive and automatic selection of the cost function parameters, and the extension of the presented reconstruction method to incorporate temporal data while retaining current processing speed.

6. Conclusion

We have presented a novel method for real-time 3D reconstruction of the guidewire from a single X-ray image. The precision of the guidewire reconstruction using a single image is limited by the thickness of the vessels in the depth direction, thus imposing usage restrictions: the reconstruction cannot be reliably utilized for any navigational tasks where the guidewire must be navigated from a large vessel to a significantly smaller side-branching vessel unless the C-arm is reoriented to place the dominant error in the direction that has no effect. The proposed method is useful for computer aided intervention that require a guidewire localization with the accuracy only up to the vessel width.

Acknowledgements

Appendix A. Real-time implementation considerations

Here we discuss selected aspects of the proposed reconstruction method that are important for achieving real-time performance. Computationally demanding stages of the proposed method include the 2D processing, the backprojection and the greedy reconstruction.

A.1. 2D processing stage

Both of the two proposed 2D processing stages are computationally intensive with the monotracker being more complex. The vesselness map computation, specifically 2D convolutions, are the computationally most demanding. All convolution kernels are separable so six 1D convolutions must be performed. To further reduce the processing demands we reproject the 3D restrictive volume and the reconstructed guidewire (if available) to the image plane thus creating a ROI that significantly limits the processing area. For the test datasets using such limited processing area typically reduces the monotracker's computational time by a factor of three. No other components of the monotracker are an not computationally significant, e.g. replacing Frangi measure with Sato [27] does not yield a significant speedup.

Measured computational times for both of the proposed 2D trackers are shown in Fig. 19.

A.2. Backprojection and 3D reconstruction stage

The backprojection is straightforward, however, there are several issues that influence accuracy and real-time performance: the choice of the ray tracing algorithm and the choice of the data structures.

The number of 2D points is negligible compared to the total number of input pixels making a CPU ray-tracing feasible. An integer only DDA (Digital Differential Analyzer) [7] like tracer is a natural choice as both image and volume data are discrete. As there usually exists a large disparity between pixel and voxel dimensions we use a supercover DDA ray-tracer. CPU only implementation

requires about 1 second to compute all intersections between rays and vasculature for a typical 1024^2 image and 256^3 volume. A lookup table is used to store the results. The look-up table is designed to enable fast retrieval based on the pixel coordinates, however, this data in raw form is not suitable for the proposed reconstruction procedure.

Critical is the design of the data structure to store the backprojection result. The data structure should fulfill the following requirements: (1) for any 3D point access to the local vessel topology must be as fast as possible, (2) for any 3D point access to the data from the 2D detection stage must be fast as possible, (3) for any 2D point access to the data from the 3D detection stage must be fast as possible, and (4) a fast access to a set of both 2D and 3D points proximal to any chosen point, with and without regard to the vessel topology, must be implemented. An additional efficiency requirement is to store all data (e.g. point coordinates) required for the cost function in compact cache-aware read-only memory blocks to reduce any fetch overhead during computation of the cost function. Several layers of redirections are required to fulfill the requirements. We assign the unique sequentially generated identifiers to every 2D and to every 3D point. Several look-up tables based on the unique identifier are used to facilitate fast constant time access to the required data. Additional redirections through the use of point identifiers achieve the following: (a) for some tasks, e.g. pre-selection of points for which to compute the cost function, only point identifiers and look-up tables are manipulated as the proximity can be inferred and (b) actual point data such as coordinates, line directions etc. is compactly stored in read-only cache aligned blocks making the proposed parallel design simpler. The proposed data organization introduces small overhead in the backprojection step, but the overhead is justifiable as it significantly reduces computational time of the reconstruction procedure.

Critical issues of the iterative parallel optimization scheme are synchronization and breadth/depth of the search. Due to the data preparation during the backprojection stage synchronization overhead is reduced; synchronization is needed only when worker threads update a shared storage. The shared storage stores the guidewire points organized in a tree (or a forest for multiple disjoint guidewires). A tree node stores one curve segment. Tree branching identifies alternative solutions. The search depth is limited by specifying the number of alternative solutions that can share the same 2D point.

An additional technique used to speed up the reconstruction is lazy evaluation of the cost function factors. Cost function factors are computed sequentially in the order of increased computational complexity. The cost function is constructed as an additive combination of non-negative factors so this approach enables fast rejection of points thus eliminating the need to compute the rest of the cost function factors. All cost function terms are computed using fast primitives provided by the Intel IPP [15].

References

[1] Alderliesten T, Konings MK, Niessen WJ. Simulation of guide wire propagation for minimally invasive vascular interventions. In: Dohi T, Kikinis R, editors. Medical image computing and computer-assisted intervention (MICCAI 2002), vol. 2489 of Lecture notes in computer science. Berlin Heidelberg: Springer-Verlag; 2002.

[2] Baert S, van de Kraats E, van Walsum T, Viergever M, Niessen W. Three-dimensional guide-wire reconstruction from biplane image sequences for integrated display in 3-d vasculature. IEEE Transactions on Medical Imaging 2003;22(10):1252–8.

[3] Baert S, Viergever M, Niessen W. Guide-wire tracking during endovascular interventions. IEEE Transactions on Medical Imaging 2003;22(8):965–72.

[4] Barbu A, Athitsos V, Georgescu B, Boehm S, Durlak P, Comaniciu D. Hierarchical learning of curves application to guidewire localization in fluoroscopy. In: IEEE conference on computer vision and pattern recognition, 2007: CVPR'07. 2007.

[5] Belyaev AG. A note on invariant three-point curvature approximations (singularity theory and differential equations). RIMS Kokyuroku 1999–2008;1111:157–64 http://ci.nii.ac.jp/naid/110000163777/en/

[6] Bismuth V, Vancamberg L, Gorges S. A comparison of line enhancement techniques: applications to guide-wire detection and respiratory motion tracking. In: Pluim JPW, Dawant BM, editors. Medical imaging 2009: image processing, vol. 7259 of Proceedings of SPIE. Society of Photo-Optical Instrumentation Engineers (SPIE); 2009.

[7] Bresenham JE. Algorithm for computer control of a digital plotter. IBM System Journal 1965;4(1):25–30.

[8] de Boor C. A practical guide to splines. New York, NY, USA: Springer-Verlag; 1998.

[9] Dietz A, Kynor DB, Friets E, Triedman J, Hammer P. Effects of uncertainty in camera geometry on three-dimensional catheter reconstruction from biplane fluoroscopic images. In: Sonka M, Fitzpatrick JM, editors. Medical imaging 2002: image processing, vol. 4684. SPIE; 2002. http://link.aip.org/link/?PSI/4684/237/1

[10] Dubuisson M-P, Jain AK. A modified Hausdorff distance for object matching. In: Proceedings of the international conference on pattern recognition. 1994.

[11] Esthappan J, Kupinski M, Lan L, Hoffmann K. A method for the determination of the 3D orientations and positions of catheters from single-plane X-ray images. In: Proceedings of the 22nd annual international conference of the IEEE engineering in medicine and biology society, vol. 3. 2000.

[12] Foley JD, van Dam A, Feiner SK, Hughes JF, Phillips RL. Introduction to computer graphics. 1st ed. Boston: Addison-Wesley; 1993.

[13] Frangi AF, Niessen WJ, Vincken KL, Viergever MA. Muliscale vessel enhancement filtering. In: MICCAI'98: proceedings of the first international conference on medical image computing and computer-assisted intervention. London, UK: Springer-Verlag; 1998.

[14] Hasegawa B. Physics of medical X-ray imaging. Medical Physics Publishing Corporation; 1987.

[15] Intel Corporation. Intel® integrated performance primitives (Intel® IPP) 6.1 – documentation. http://software.intel.com/en-us/articles/intel-integrated-performance-primitives-documentation/

[16] Intel Corporation. Intel® math kernel library reference manual. http://developer.intel.com

[17] Koller TM, Gerig G, Székely G, Dettwiler D. Multiscale detection of curvilinear structures in 2-D and 3-D image data. In: Proceedings of the fifth international conference on computer vision (ICCV'95). Cambridge, Massachusetts, USA: IEEE Computer Society; 1995.

[18] Lessard S, Lau C, Chav R, Soulez G, Roy D, de Guise JA. Guidewire tracking during endovascular neurosurgery. Medical Engineering & Physics 2010;32(8):813–21 http://www.sciencedirect.com/science/article/pii/S1350453310001116

[19] Li F, Leung MKH, Yu X. A two-level matching scheme for speedy and accurate palmprint identification. In: Advances in multimedia modeling, vol. 4352 of Lecture notes in computer science. Berlin/Heidelberg: Springer; 2006. http://www.springerlink.com/content/x36705560h0vuu2p/

[20] Mazouer P, Chen T, Zhu Y, Wang P, Durlak P, Thiran J-P, et al. User-constrained guidewire localisation in fluoroscopy. In: Pluim JPW, Dawant BM, editors. Medical imaging 2009: image processing, vol. 7259 of Proceedings of SPIE. Society of Photo-Optical Instrumentation Engineers (SPIE); 2009.

[21] Minnote MC. Nonparametric testing of the existence of modes. The Annals of Statistics 1997;25(4):1646–60.

[22] Neumaier A. Complete search in continuous global optimization and constraint satisfaction. Acta Numerica 2004;13(1):271–369.

[23] Palti-Wasserman D, Burkstein AM, Beyar RP. Identifying and tracking a guide wire in the coronary arteries during angioplasty from X-ray images. IEEE Transactions on Biomedical Engineering 1997;44(2): 152–64.

[24] Petković T, Lončarić S. Guidewire tracking with projected thickness estimation. In: 2010 IEEE international symposium on biomedical imaging: from nano to macro. IEEE; 2010.

[25] Petković T, Lončarić S. Using X-ray imaging model to improve guidewire detection. In: 2010 IEEE 10th international conference on signal processing. IEEE; 2010.

[26] Petković T, Lončarić S, Devčić T, Homan R. Non-iterative guidewire reconstruction from multiple projective views. In: Lončaric S, Ramponi G, Šeršić D, editors. 7th international symposium on image and signal processing and analysis (ISPA 2011). Dubrovnik: University of Zagreb; 2011.

[27] Sato Y, Nakajima S, Shiraga N, Atsumi H, Yoshida S, Koller T, et al. Three-dimensional multi-scale line filter for segmentation and visualization of curvilinear structures in medical images. Medical Image Analysis 1998;2(2):149–68.

[28] Silverman BW. Using kernel density estimates to investigate multimodality. Journal of the Royal Statistical Society, Series B (Methodological) 1981;43(1):97–9.

[29] Söderman M, Babić D, Homan R, Andersson T. 3d roadmap in neuroangiography: technique and clinical interest. Neuroradiology 2005;47(10):735–40 http://www.springerlink.com/content/g867p11160128294/

[30] Spiegel M, Pfister M, Hahn D, Daum V, Hornegger J, Struffert T, et al. Towards real-time guidewire detection and tracking in the field of neuroradiology. In: Miga MI, Wong KH, editors. Medical imaging 2009: visualisation, image-guided procedures, and modelling, vol. 7261 of Proceedings of SPIE. Society of Photo-Optical Instrumentation Engineers (SPIE); 2009.

[31] Steger C. An unbiased detector of curvilinear structures. IEEE Transactions on Pattern Analysis and Machine Intelligence 1998;20(2):113–25.

[32] Takemura A, Hoffmann KR, Suzuki M, Wang Z, Rangwala HS, Harauchi H, et al. An algorithm for tracking microcatheters in fluoroscopy. Journal of Digital Imaging 2008;21(1):99–108.

[33] van Walsum T, Baert S, Niessen W. Guide wire reconstruction and visualization in 3DRA using monoplane fluoroscopic imaging. IEEE Transactions on Medical Imaging 2005;24(5):612–23.

[34] Wang P, Zhu Y, Chen T, Durlak P, Bill U, Comaniciu D. Hierarchical guidewire tracking in fluoroscopic sequences. In: Pluim JPW, Dawant BM, editors. Medical imaging 2009: image processing, vol. 7259 of Proceedings of SPIE. Society of Photo-Optical Instrumentation Engineers (SPIE); 2009.

[35] Watt AH. 3D computer graphics. 3rd ed. Harlow, England: Addison-Wesley; 1999.

[36] Weickert J. Coherence-enhancing diffusion filtering. International Journal of Computer Vision 1999;31(2–3):111–27, http://dx.doi.org/10.1023/A:1008009714131.

[37] Zarge JA, Corby NR. Method and apparatus for real-time tracking of catheter guide wires in fluoroscopic images during interventional radiological procedures. U.S. Patent 5,289,373; 1994 [General Electric Company].